Joint reconstruction of an in-focus image and of the background signal in in-line holographic microscopy

Anthony Berdeu, Thomas Olivier, Fabien Momey, Loïc Denis, Frédéric Pinston, Nicolas Faure, Corinne Fournier

Version of Record: https://www.sciencedirect.com/science/article/pii/S0143816621001615
Manuscript_c94b07826a141c2de167ad8dcc324538

Joint reconstruction of an in-focus image and of the background signal in in-line holographic microscopy*

Anthony Berdeu[a], Thomas Olivier[a], Fabien Momey[a,*], Loïc Denis[a], Frédéric Pinston[b], Nicolas Faure[b] and Corinne Fournier[a]

[a]Univ Lyon, UJM-Saint-Etienne, CNRS, Institut d Optique Graduate School, Laboratoire Hubert Curien UMR 5516, F-42023, Saint-Etienne, France
[b]bioMérieux, 5 rue des Berges, 38024 Grenoble cedex 01, France

ARTICLE INFO

Keywords:
Digital holography
Image reconstruction
Inverse problems

ABSTRACT

In-line digital holography is a simple yet powerful tool to image absorbing and/or phase objects. However, the holograms of interest are perturbed by the background signal due to unwanted scattering elements located in the optical path.

Using only two holograms of the same object, shifted to different locations, an inverse problems approach is applied to jointly estimate the complex transmittance of the sample and the contribution of the interferent background signal at the sensor plane. Experimental results with stained bacteria are presented and show improved reconstructions of the sample while also accounting for the background contribution.

1. Introduction

In-line holographic setups [1] are much simpler and less sensitive to vibrations than off-axis setups. As illustrated in Fig. 1(a), in-line holography simply consists in recording the intensity of the patterns diffracted by all the elements located in the optical path of a coherent light beam. In holographic microscopy, an objective and other optical elements (not represented in this simplified figure) are placed between the object and the sensor to obtain a magnified image of the sample. After numerical reconstruction, this technique enables access to the absorption and phase shift of the objects, making it particularly suitable for studying absorbing as well as transparent objects in many domains including biology [2], fluid mechanics [3] and for particle characterization [4].

By applying the diffraction equations [5], the diffracted wave can be back propagated to the object plane quite simply. However, the reconstructed wave is often distorted due to the diffraction of unwanted out-of-focus objects, such as dust on the optical elements, giving rise to a "background signal" (cf. Fig. 1). Background correction in in-line holography is problematic because the sensor is sensitive to the intensity of the interferences between the wavefront scattered by the sample of interest and this unwanted background. Standard reconstruction techniques assume that these interferences are negligible, so that the diffraction patterns due to the objects and those that form the background can be incoherently summed. Standard background corrections are performed by subtracting a background hologram from the sample hologram. These corrections are used to compensate for illumination inhomogeneities [6, 7] or to remove out-of-focus objects perturbations [2, 8, 9]. The background hologram can be either: (i) captured by acquiring a hologram after shifting the objects out of the field of view, (ii) computed by averaging a hologram sequence of moving objects [2, 7, 9], (iii) computed by low-pass filtering of a single hologram [6, 8]. Solution (i) requires that a part of the glass slide be free of objects of interest to only capture the contribution of the out-of-focus objects that remain static whatever the glass slide position (cf. Fig. 1). Solution (ii) requires sufficiently long hologram video and sufficient motion of the objects of interest to ensure each point in the field of view to be most of the time free of objects. Solution (iii) is analog to high-pass filtering the hologram before reconstruction, which leads to a loss of information and cannot suppress the high frequency fringes of unwanted objects in the optical path. In addition, none of these solutions account for the interferences between the background wavefront and the wavefront scattered by the objects of interest, by assuming a simple summation of their respective intensity.

In the proposed method, we apply a different strategy: joint reconstruction of the background and of the sample of interest, using an inverse problems approach. In order to separate the objects and the background, we use two holograms acquired at two different locations of the sample (either longitudinal or lateral shifts or both). In these two holograms, the background structures, fixed in the optical path of the setup, remain at the same location. The inverse problems framework is based on an image formation model that accounts for the interference between the object wave and the background, to reduce twin-image artifacts, and to improve the reconstruction of the absorption and phase images.

2. Proposed method

Inverse problems methods reconstruct an image by considering both an optical model (the forward model) of the hologram formation and some prior knowledge about the

*Funding. French National Research Agency (ANR) (LABEX PRIMES of Université de Lyon ANR-11-LABX-0063, Investissements d'Avenir ANR-11-IDEX-0007); Region Auvergne-Rhônes-Alpes (project DIAGHOLO).
*Corresponding author
fabien.momey@univ-st-etienne.fr (F. Momey)
ORCID(s):

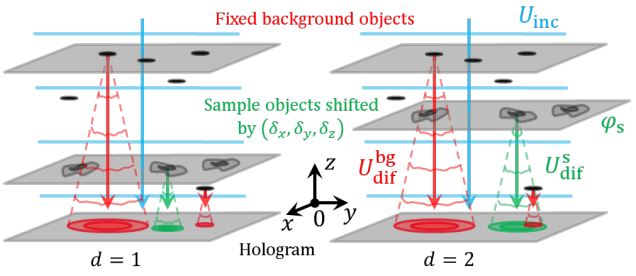

Figure 1: Hologram formation principle in the presence of disturbing objects (black circles): background patterns originate from dust (top, red), the 2D sample diffracts light (middle, green), in the sensor plane a hologram is captured (bottom). Optical elements are not shown here, and a fixed background plane accounts for all the disturbances. Between acquisitions 1 and 2, the sample is shifted.

sample. These methods iteratively reduce the discrepancies between the modeled hologram and the data [10, 11, 12]. We use this general framework to jointly retrieve the sample and the background signal using two holograms. As illustrated in Fig. 1, between the two acquisitions, the objects of interest (green) are shifted by $(\delta_x, \delta_y, \delta_z)$. The background (red) is assumed to remain unchanged, which is the case of patterns created by dust adhering to the setup interfaces such as lenses or filters. The background and the objects are unmixed thanks to the reconstruction process.

2.1. Forward model

A 2D complex transmittance plane $\underline{t}(x, y) = \exp\left(i\underline{\varphi}(x, y)\right)$ is completely described by its complex phase $\underline{\varphi} = \varphi_r + i\varphi_i$, where complex values are underlined for the sake of clarity. With this convention, the real and imaginary parts of $\underline{\varphi}$ are directly linked to the complex refractive index of the transmittance plane whose real part accounts for the phase delay it introduces and whose imaginary part accounts for its absorption.

As shown in Fig. 1, under the first Born approximation [5] (single scattering hypothesis), the forward model accounts for the interferences between three waves: the incident (unperturbed) wave $\underline{U}_{\text{inc}}$ (blue), the wave diffracted by background objects $\underline{U}^{\text{bg}}_{\text{dif}}$ (red), and the wave diffracted by the sample $\underline{U}^{\text{s}}_{\text{dif}}$ (green). The interference of the incident and background waves is modeled on the sensor plane by a single term $\exp(i\underline{\varphi}_{\text{bg}})$ which corresponds to a non uniform wave with a wavefront distorted by propagation through the background objects. The objects of interest, located in the sample plane, induce a phase shift noted $\underline{\varphi}_{\text{s}}$. The model consequently depends on the complex phases $\Phi = (\underline{\varphi}_{\text{bg}}, \underline{\varphi}_{\text{s}})$ defined respectively in the sensor and sample planes as well as on a set of geometrical parameters $\rho = (z, \delta_x, \delta_y, \delta_z)$. These geometrical parameters are the distance z between the sample and the sensor during the first acquisition and the 3D shift performed before the second acquisition $(\delta_x, \delta_y, \delta_z)$.

As under first Born approximation the complex transmittance of the object plane is considered to be illuminated by an unperturbed plane incident wave, the location of the background transmittance plane can be set arbitrarily. Therefore, it can be considered before or after the object plane without changing the imaging model. For the sake of simplicity, we place this plane at the sensor plane in the following. Considering a monochromatic plane wave illumination $\underline{U}_{\text{inc}}(z) = \exp(-ikz)$ of wavelength λ, wavenumber $k = 2\pi/\lambda$, its propagation can be described by the first Rayleigh-Sommerfeld solution [5, Section 3.5.1]. The corresponding Rayleigh-Sommerfeld propagator [12] at propagation distance z is:

$$\underline{h}_z(x, y) = \frac{1}{i\lambda}\frac{z}{r}\left(1 - \frac{1}{ikr}\right)\frac{e^{ikr}}{r} \text{ with } r^2 = x^2+y^2+z^2\,, \quad (1)$$

and the complex amplitude on the sensor plane can be modeled, for the first acquisition $d = 1$, by:

$$\underline{U}_1(\Phi, \rho) = \underbrace{e^{i\underline{\varphi}_{\text{bg}}}}_{\underline{U}_{\text{inc}}(0)+\underline{U}^{\text{bg}}_{\text{dif}}} + \underbrace{\underline{U}_{\text{inc}}(z)\left(e^{i\underline{\varphi}_{\text{s}}} - 1\right) * \underline{h}_z(x, y)}_{\underline{U}^{\text{s}}_{\text{dif}}}\,. \quad (2)$$

The term $\left(e^{i\underline{\varphi}_{\text{s}}} - 1\right)$ models only the light diffracted by the sample plane (first Born approximation). The term $e^{i\underline{\varphi}_{\text{bg}}}$ takes into account both the plane wave illumination contribution and the background contribution by modeling their interference.

For the second acquisition $d = 2$, the shift is to be taken into account:

$$\underline{U}_2(\Phi, \rho) = e^{i\underline{\varphi}_{\text{bg}}} + \underline{U}_{\text{inc}}(z)\left(e^{i\underline{\varphi}_{\text{s}}} - 1\right) * \underline{h}_{z+\delta_z}\left(x + \delta_x, y + \delta_y\right)\,. \quad (3)$$

Finally, the forward model of the intensity measured by the sensor for acquisition $d = 1$ or 2 is:

$$\tilde{I}_d(\Phi, \rho) = \left|\underline{U}_d(\Phi, \rho)\right|^2\,. \quad (4)$$

2.2. Inverse problems formulation

Estimating parameters ρ and reconstructing the images Φ can be stated as a regularized minimization problem involving the residuals between the data intensity $\{I_d\}_{d=1..2}$ and its model $\{\tilde{I}_d(\Phi, \rho)\}_{d=1..2}$:

$$\begin{aligned}(\hat{\Phi}, \hat{\rho}) = \underset{\Phi\in\mathscr{D},\,\rho}{\operatorname{argmin}}\ & \mathscr{C}^W_{\text{data}}\left(I_1, \tilde{I}_1(\Phi, \rho)\right) \\ & + \mathscr{C}^W_{\text{data}}\left(I_2, \tilde{I}_2(\Phi, \rho)\right) \\ & + \mu_{\text{sp,s}}\mathscr{C}_{\text{sp}}\left(\underline{\varphi}_{\text{s}}\right) \\ & + \mu_{\text{sm,s}}\mathscr{C}_{\text{sm}}\left(\underline{\varphi}_{\text{s}}\right) \\ & + \mu_{\text{sm,bg}}\mathscr{C}_{\text{sm}}\left(\underline{\varphi}_{\text{bg}}\right)\,. \end{aligned} \quad (5)$$

The term $\mathscr{C}^{W}_{\text{data}} = \min_{c} \sum_{j,\ell} \left(\left[I_d\right]_{j,\ell} - c \left[\tilde{I}_d\right]_{j,\ell} \right)^2 [W]_{j,\ell}$ is the data fidelity term, where (j,ℓ) stands for the sensor pixels locations and c is a real-valued coefficient to adjust the range of the model to the data acquisition dynamic, and W is a map of weighting coefficients accounting for either the unmeasured pixels or the limited size of the sensor [12, 13].

Regularization terms $\mathscr{C}_{\text{sp}}$ and $\mathscr{C}_{\text{sm}}$ applied on $\underline{\varphi}_{\text{bg}}$ and $\underline{\varphi}_{\text{s}}$ are weighted by hyperparameters $\mu_{\text{sp,s}}$, $\mu_{\text{sm,s}}$ and $\mu_{\text{sm,bg}}$.

$\mathscr{C}_{\text{sp}}\left(\underline{\varphi}\right) = \sum_{j,\ell} \left|\left[\varphi_{\text{r}}\right]_{j,\ell}\right| + \tau_1 \left|\left[\varphi_{\text{i}}\right]_{j,\ell}\right|$, the weighted sum of the ℓ_1-norms of φ_{r} and φ_{i}, ensures the sparsity of the reconstructed sample image $\underline{\varphi}_{\text{s}}$, which prevents twin-image artifacts [10] by favoring objects with compact supports, i.e., such that $\underline{\varphi}_{\text{s}}$ is zero at many pixels of the sample plane where no absorption or phase shift occur. Since this sparsity prior can bias the reconstruction [14], it is debiased using the method proposed in [15].

$\mathscr{C}_{\text{sm}}\left(\underline{\varphi}\right) = \sum_{j,\ell} \Delta^2_{j,\ell}\left[\varphi_{\text{r}}\right] + \tau_2 \Delta^2_{j,\ell}\left[\varphi_{\text{i}}\right]$ smooths the reconstructed phases by favoring low-energy spatial gradients, which prevents noise amplification [12]. $\Delta^2_{j,\ell}[\,\cdot\,] = \left([\,\cdot\,]_{j+1,\ell} - [\,\cdot\,]_{j,\ell}\right)^2 + \left([\,\cdot\,]_{j,\ell+1} - [\,\cdot\,]_{j,\ell}\right)^2$ corresponds to a finite difference operator.

Hyper-parameters τ_1 and τ_2 are introduced to account for the different ranges of the real and imaginary parts φ_{r} and φ_{i}, they have a limited influence and can be set once for all.

Finally, $\Phi \in \mathscr{D}$ are the constraints on the domain of the set Φ. In our case, $\Phi \in \mathscr{D} \Leftrightarrow \mathfrak{Im}\left([\underline{\varphi}_{\text{s}}]_{j,\ell}\right) \geq 0$, i.e. we impose the positivity of the objects' absorbance. This constraint is justified by the fact that objects cannot emit light in the wave propagation process. Conversely, no hard constraint is enforced on the domain of the background that is thus allowed to fluctuate positively and negatively to account for any illumination inhomogeneity.

2.3. Alternating minimization algorithm and initialization

Solving (5) provides the complex phases Φ jointly with the parameters ρ. In practice, we alternate a minimization step with respect to Φ (with ρ fixed to its previous estimation) and a second with respect to ρ (with Φ fixed to its previous estimation). The reconstructions of Φ with ρ fixed are performed by a limited-memory quasi-Newton method with bound constraints, VMLM-B [12, 16]. The regularization hyperparameters $\mu_{\text{sp,s}}$, $\mu_{\text{sm,s}}$ and $\mu_{\text{sm,bg}}$ are tuned empirically to obtain the best visual reconstruction quality. The optimizations of ρ with Φ fixed are done via a simplex search method [17]. The method is implemented in the GlobalBioIm framework [18, 19].

Parameters ρ are initialized based on the simple back-propagated transmittances $\underline{t}_1$ and $\underline{t}_2$ of the holograms. The initial lateral shifts $\left(\delta_x, \delta_y\right)$ are first estimated by rigid registration of $\underline{t}_1$ and $\underline{t}_2$. The initial focus distances z and $z+\delta_z$ are obtained by maximizing the sharpness of $\left|\underline{t}_d - 1\right|$ [20], a focusing criterion that works for both absorbing and dephasing objects.

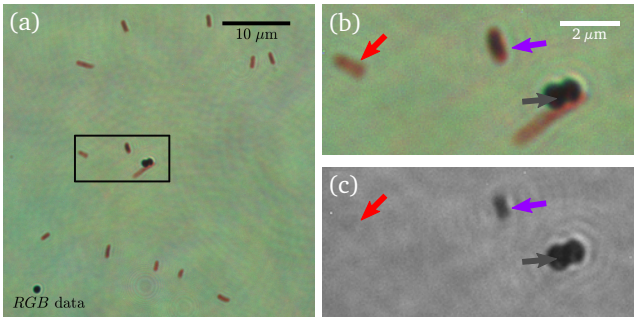

Figure 2: (a) Bright-field image of Gram-stained bacteria. (b) Zoomed-in view. (c) Under red illumination, absorbing, translucent and weakly absorbing bacteria are respectively identified with black, red and purple arrows.

3. Results

The proposed method was tested on Gram-stained bacteria, fixed on a slide, using a standard procedure (bioMérieux PreviColor Gram system): Gram-positive cocci Staphylococcus epidermidis (*S. epidermidis*) and Gram-negative rods Escherichia coli (*E. coli*), see Fig. 2.

The data were acquired via a microscope (Olympus BX-61, oil-immersion 60x/NA1.4 objective, 10x tube lens, Basler monochromatic camera with a pixel pitch 3.45 μm) [11]. The illumination source was a fiber-coupled red LED (617 nm, Mightex FCS-0617-000), filtered by a 5 nm band-pass filter centered at 610 nm. The tip of the fiber was placed approximately 5 centimeters from the sample. A (x, y, z) motorized stage was used to shift the sample.

Two reconstruction experiments were performed from two acquired datasets: one for which the second hologram has been laterally shifted relatively to the first hologram, and one for which the two holograms have been acquired at two different defocus distances (*i.e.* axial shift). Figure 3 and Figure 4 present the hologram data used in our experiments and estimation results in the data space. Figure 5 illustrates reconstruction results in the object space (information of interest). Each figure is detailed hereafter. A compilation of all the presented images (data, background estimation, sample estimation in the data and object spaces, residuals), for each experiment, are proposed in two respective supplementaries that are referred as Visualization 1 and Visualization 2.

Figure 3(a) shows the first of two holograms acquired with the same defocus of $z = 8$ μm and a lateral shift of $\delta_x = 5$ μm (see Visualization 1). Figure 4(a) shows two holograms acquired at two different defocus of respectively $z = 8$ μm and $z = 16$ μm (see Visualization 2).

In the hologram in Fig. 3(a), diffraction patterns can be seen at the location of absorbing (purple and black arrows) or transparent (red arrow) objects, perturbed by the background texture. Figures 5(a)-5(b) show a simple back propagation. The contrast is weak because of the corruption by the background structures and the twin-image noise. The transparent

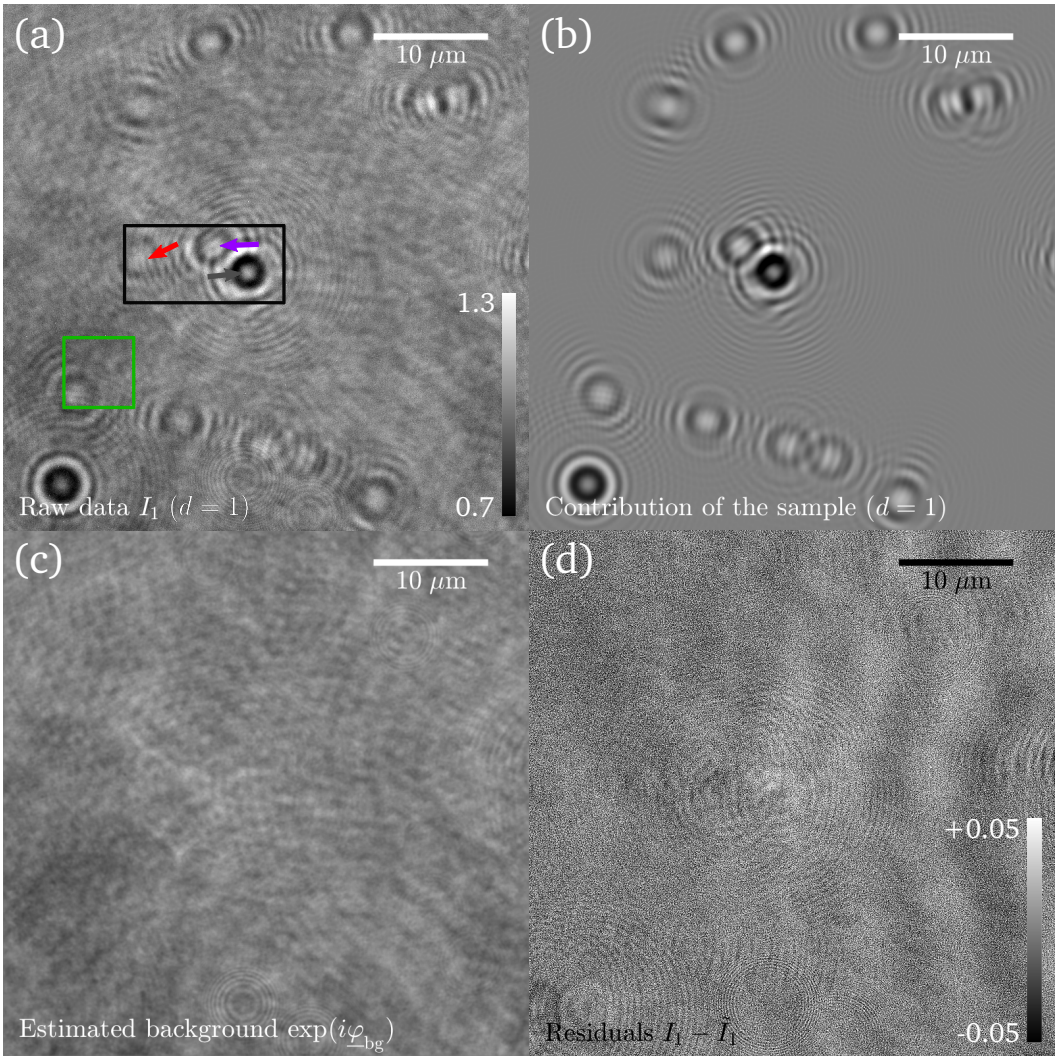

Figure 3: (a) An in-line hologram of the bacteria shown in Fig. 2(a). The green frame emphasizes a darker region in the perturbed background. The colored arrows point at the diffraction patterns produced by the objects highlighted in Fig. 2. A pair of holograms recorded with a lateral shift of the sample is reconstructed. The contribution of the retrieved object $\underline{\varphi}_s$ is shown in (b) and the background signal in (c) with the same color bar as in (a). (d) gives the residuals $I_1 - \tilde{I}_1$ between the first hologram and the predicted intensity.

bacteria can hardly be seen in the phase image, as zoomed in Fig. 5(j).

In the proposed method, the spatial coherence of the illumination source and other resolution-limiting factors such as the numerical aperture are included in the forward model [21]. Given that the refractive index of the bacteria is larger than that of the surrounding medium, a positivity constraint is also applied on the real part of $\underline{\varphi}_s$, enforcing a positive phase shift.

Figures 5(c)-5(d) show the sample retrieved using a standard inverse problems approach [11], that aims at applying the proposed approach without estimating the background contribution: $\Phi \in \mathscr{D} \Rightarrow \underline{\varphi}_{\text{bg}} = 0$, all other things being equal. The result suggests that the darker region, framed in green, strongly pollutes the retrieved modulus and phase, even when two shifted holograms are used in the reconstruction. This shows that when the background signal is strong, standard reconstruction methods in digital holography microscopy such as, among others, modified Gerchberg-Saxton algorithms [22, 23], regularized approaches with priors [24], inverse problem approaches from multiple holograms [25] or even single hologram [11], bias the reconstruction of the object of interest, as they do not account for the background contribution.

Finally, Figs. 5(e)-5(f) and Figs. 5(g)-5(h) present the sample reconstructed with the proposed method, respectively for laterally shifted acquisitions and for acquisitions with different defocus. Compared to Figs. 5(a)-5(b), the sample absorption, given in Fig. 5(e)-5(g), and the sample phase, given in Fig. 5(f)-5(h), are almost free from background perturbations or twin-image artifacts, as is particularly visible in the region framed in green. The transparent objects appear to be well segmented in the phase image.

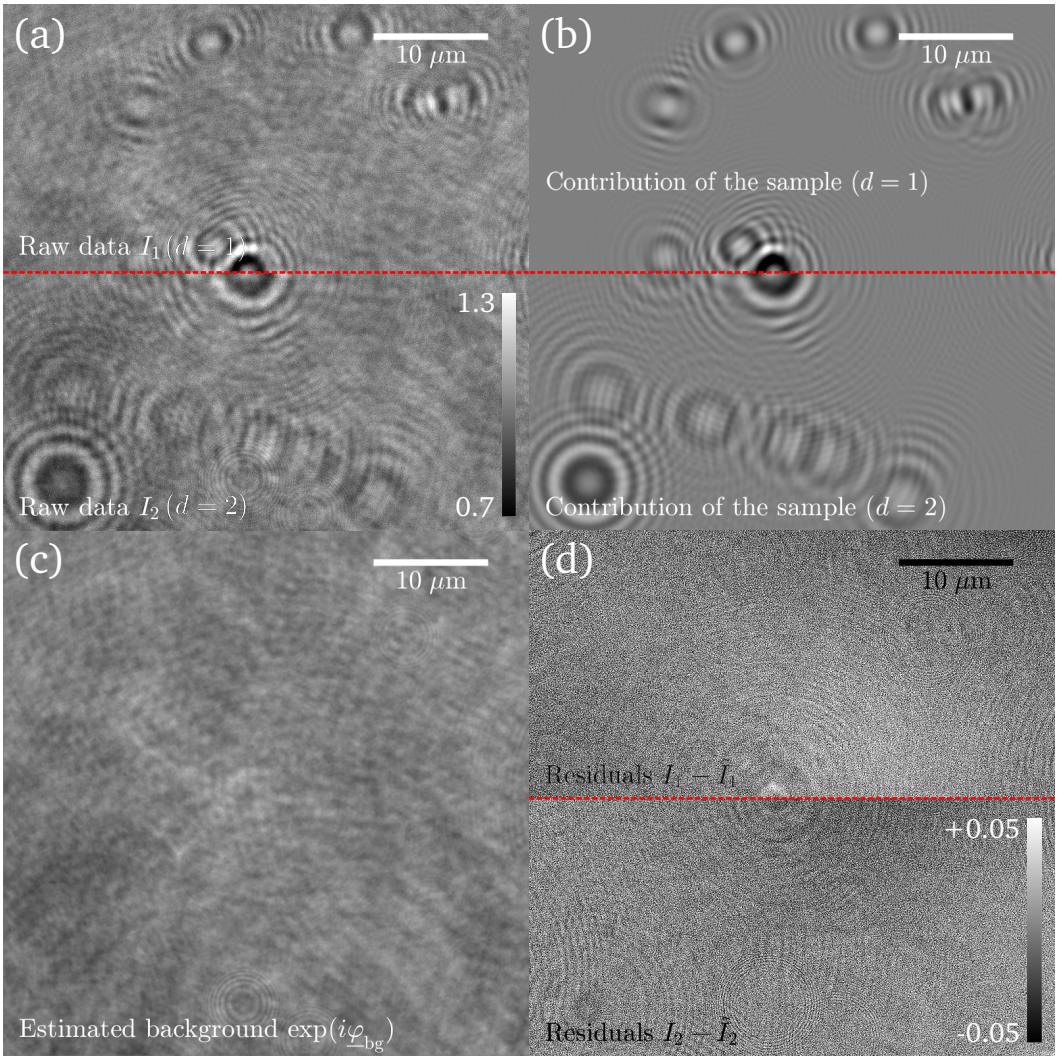

Figure 4: (a) A pair of in-line holograms of the bacteria shown in Fig. 2(a), acquired at 2 different defocus distance. (a,b,d) We visualize both holograms respectively on the upper and lower half parts of the field of view (separated by a red dashed line). This pair of holograms is reconstructed. The contribution of the retrieved object $\underline{\varphi}_s$ at the 2 corresponding defocus are shown in (b) and the background signal in (c) with the same color bar as in (a). (d) gives the residuals $I_1 - \tilde{I}_1$ and $I_2 - \tilde{I}_2$ between the holograms and the predicted intensity.

The contrast of the phase objects is enhanced compared with simple back propagation Fig. 5(b), and the objects are better localized. Some faint artifacts remain in the phase around strongly absorbing objects.

Comparing Fig. 3(a) with Figs. 3(b)-3(c) and Fig. 4(a) with Figs. 4(b)-4(c), the proposed method successfully unmixes the signal produced by the object of interest from the background. The objects and the background are clearly separated, with minimal cross-contamination between Fig. 3(b) and Fig. 3(c), and between Fig. 4(b) and Fig. 4(c). The residuals of Fig 3(d) and Fig 4(d) are below 5 % of the original dynamic range. Although some high frequency structures are faintly visible, the main unexplained global structures are large vertical fringes in the illumination. They may be due to the glass slide and hence move with the sample, which prevents them from being separated from the signal of interest.

Table 1 shows that, in contrast to the lateral shift initialization that is very precise with corrections of only 10 nm, the initial auto-focus distance (estimated as described in Sec. 2.3) is overestimated: the correction after several iterations of our alternating minimization algorithm exceeds 140 nm. Some tests (not shown here) show that the refinement of the focus distance is beneficial to the reconstructions.

Table 1
Estimates of the different parameters ρ at the beginning and at convergence of our alternating minimization algorithm.

ρ	**Initial** (μm)	**Final** (μm)	**Difference** (nm)
δ_x / δ_y	4.48 / 0.11	4.47 / 0.12	-10 / 10
z / $z+\delta_z$	7.80 / 7.72	7.62 / 7.58	-180 / -140

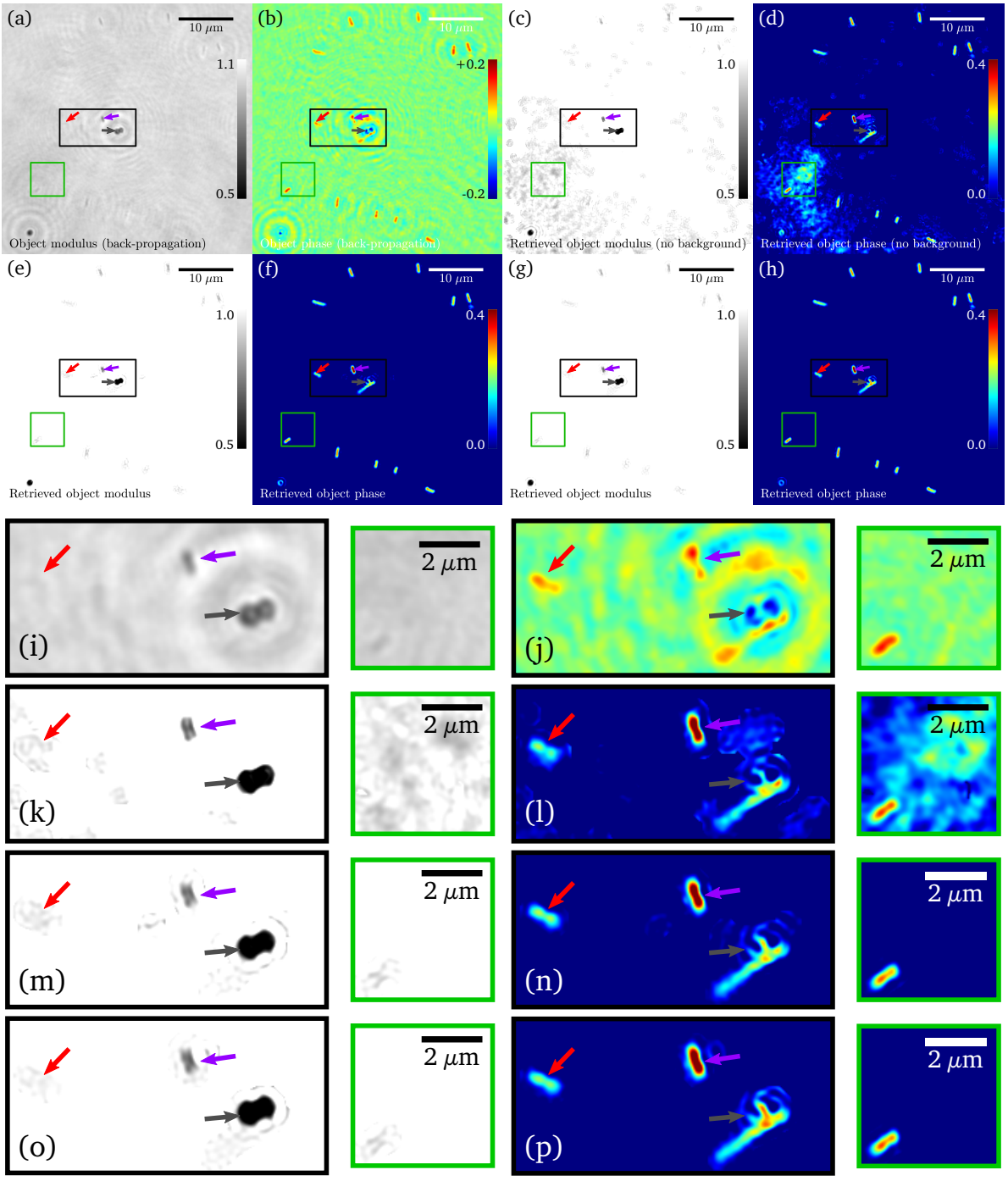

Figure 5: (a,b) Modulus and phase (radian) obtained with a simple back-propagation of Fig. 3(a). (c,d) Modulus and phase (radian) of the retrieved sample $\underline{\varphi}_{\mathrm{s}}$ without the estimation of the background $\underline{\varphi}_{\mathrm{bg}}$ via a state-of-the-art inverse problem approach. (e,f) Modulus and phase (radian) of the retrieved sample $\underline{\varphi}_{\mathrm{s}}$ with the proposed method, from two laterally shifted holograms. (g,h) Modulus and phase (radian) of the retrieved sample $\underline{\varphi}_{\mathrm{s}}$ with the proposed method, from two holograms acquired at two different defocus. (i,j,k,l,m,n,o,p) Zooms of (a,b,c,d,e,f,g,h). For full resolution, see Visualization 1 and Visualization 2.

4. Discussion and conclusion

In this paper, we focused on the reconstruction of objects of interest that are shifted relative to a fixed background in digital holography microscopy. We have shown that an inverse problems approach jointly estimating this background signal and the signal of interest can effectively unmix these two components, using only two shifted in-line holograms as input. This separation is achieved by inverting the forward model that accounts for the interferences between the two signals. This also makes possible a refinement of the focus distance. The transparent objects are correctly reconstructed

in the sample phase.

This procedure was applied on two 2D laterally or axially shifted (differently defocused) holograms. It can be naturally extended to a higher number of acquisitions or to objects moving in front of a static background (such as microscopy of in-flow objects).

The remaining high frequency fringes in the residues indicate that there is still some room for improvements. They might be reduced by further refining the focus or the coherence length estimation or by considering a more complex modeling of hologram formation.

Finally, the different parameters such as $\mu_{\text{sp,s}}$, $\mu_{\text{sm,s}}$ and $\mu_{\text{sm,bg}}$ are currently manually set. Methods to automatically tune these hyperparemeters could be investigated.

References

[1] D. Gabor. A new microscopic principle. Nature, 161:777–778, May 1948.

[2] J. Garcia-Sucerquia, W. Xu, S. K. Jericho, P. Klages, M. H. Jericho, and H. J. Kreuzer. Digital in-line holographic microscopy. Applied Optics, 45(5):836–850, 2006.

[3] Joseph Katz and Jian Sheng. Applications of holography in fluid mechanics and particle dynamics. Annual Review of Fluid Mechanics, 42:531–555, 12 2009.

[4] S. H. Lee, Y. Roichman, G. R. Yi, S. H. Kim, S. M. Yang, A. van Blaaderen, P. van Oostrum, and D. G. Grier. Characterizing and tracking single colloidal particles with video holographic microscopy. Optics Express, 15(26):18275–18282, Dec 2007.

[5] Joseph W. Goodman. Introduction to Fourier optics. Roberts, Englewood (Colorado), 2005.

[6] W. Xu, M. H. Jericho, I. A. Meinertzhagen, and H. J. Kreuzer. Digital in-line holography of microspheres. Applied Optics, 41(25):5367–5375, Sep 2002.

[7] Mozhdeh Seifi, Corinne Fournier, Nathalie Grosjean, Loic Méès, Jean-Louis Marié, and Loic Denis. Accurate 3d tracking and size measurement of evaporating droplets using in-line digital holography and "inverse problems" reconstruction approach. Opt. Express, 21(23):27964–27980, Nov 2013.

[8] William H. Carter and Pin-Chin Ho. Reconstruction of inhomogeneous scattering objects from holograms. Applied Optics, 13(1):162–172, Jan 1974.

[9] Laszlo Orzo, Andras Feher, and Szabolcs Tokes. Advanced background elimination in digital holographic microscopy. International Workshop on Cellular Nanoscale Networks and their Applications, pages 1–5, 08 2012.

[10] Loïc Denis, Dirk Lorenz, Eric Thiébaut, Corinne Fournier, and Dennis Trede. Inline hologram reconstruction with sparsity constraints. Optics Letters, 34(22):3475–3477, Nov 2009.

[11] Frédéric Jolivet, Fabien Momey, Loïc Denis, Loïc Méès, Nicolas Faure, Nathalie Grosjean, Frédéric Pinston, Jean-Louis Marié, and Corinne Fournier. Regularized reconstruction of absorbing and phase objects from a single in-line hologram, application to fluid mechanics and micro-biology. Optics Express, 26(7):8923–8940, Apr 2018.

[12] Anthony Berdeu, Olivier Flasseur, Loïc Méès, Loïc Denis, Fabien Momey, Thomas Olivier, Nathalie Grosjean, and Corinne Fournier. Reconstruction of in-line holograms: combining model-based and regularized inversion. Opt. Express, 27(10):14951–14968, May 2019.

[13] F. Soulez, L. Denis, C. Fournier, E. Thiebaut, and C. Goepfert. Inverse-problem approach for particle digital holography: accurate location based on local optimization. Journal of the Optical Society of America. A, 24(4):1164–1171, Apr 2007.

[14] Charles-Alban Deledalle, Nicolas Papadakis, and Joseph Salmon. On Debiasing Restoration Algorithms: Applications to Total-Variation and Nonlocal-Means. Springer International Publishing, pages 129–141, 2015.

[15] Mário AT Figueiredo, Robert D Nowak, and Stephen J Wright. Gradient projection for sparse reconstruction: Application to compressed sensing and other inverse problems. IEEE Journal of selected topics in signal processing, 1(4):586–597, 2007.

[16] Eric Thiebaut. Optimization issues in blind deconvolution algorithms. Proceedings of SPIE, 4847:4847 – 4847 – 10, 2002.

[17] Jeffrey Lagarias, James A. Reeds, Margaret H. Wright, and Paul Wright. Convergence properties of the nelder–mead simplex method in low dimensions. SIAM Journal on Optimization, 9:112–147, 12 1998.

[18] Michael Unser, Emmanuel Soubies, Ferréol Soulez, Michael McCann, and Laurène Donati. GlobalBioIm: A Unifying Computational Framework for Solving Inverse Problems. Imaging and Applied Optics, CTu1B.1, 2017.

[19] Emmanuel Soubies, Ferréol Soulez, Michael McCann, Thanh-An Pham, Laurène Donati, Thomas Debarre, Daniel Sage, and Michael Unser. Pocket guide to solve inverse problems with globalbioim. Inverse Problems, 2019.

[20] Yibo Zhang, Hongda Wang, Yichen Wu, Miu Tamamitsu, and Aydogan Ozcan. Edge sparsity criterion for robust holographic autofocusing. Optics Letters, 42(19):3824–3827, Oct 2017.

[21] Stijn Vandewiele, Filip Strubbe, Caspar Schreuer, Kristiaan Neyts, and Filip Beunis. Low coherence digital holography microscopy based on the lorenz-mie scattering model. Optics express, 25(21):25853–25866, 2017.

[22] Yan Zhang, Giancarlo Pedrini, Wolfgang Osten, and Hans J. Tiziani. Reconstruction of in-line digital holograms from two intensity measurements. Optics Letters, 29(15):1787–1789, Aug 2004.

[23] C. Allier, S. Morel, R. Vincent, L. Ghenim, F. Navarro, M. Menneteau, T. Bordy, L. Hervé, O. Cioni, X. Gidrol, Y. Usson, and J.-M. Dinten. Imaging of dense cell cultures by multiwavelength lens-free video microscopy. Cytometry Part A, 91(5):433–442, 2017.

[24] Y. Rivenson, Y. Wu, H. Wang, Y. Zhang, A. Feizi, and A. Ozcan. Sparsity-based multi-height phase recovery in holographic microscopy. Scientific Reports, 6:37862, Nov 2016.

[25] L. Herve, O. Cioni, P. Blandin, F. Navarro, M. Menneteau, T. Bordy, S. Morales, and C. Allier. Multispectral total-variation reconstruction applied to lens-free microscopy. Biomedical Optics Express, 9(11):5828–5836, Nov 2018.